

Molecular Physics



An International Journal at the Interface Between Chemistry and Physics

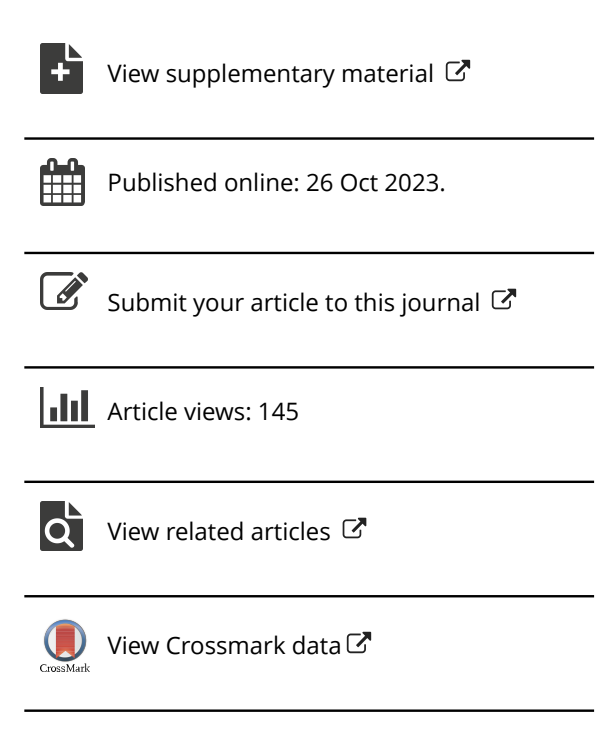
ISSN: (Print) (Online) Journal homepage: www.tandfonline.com/journals/tmph20

Size effects on polaron formation in lead chloride perovskite thin films

David R. Graupner & Dmitri S. Kilin

To cite this article: David R. Graupner & Dmitri S. Kilin (26 Oct 2023): Size effects on polaron formation in lead chloride perovskite thin films, Molecular Physics, DOI: 10.1080/00268976.2023.2273418

To link to this article: https://doi.org/10.1080/00268976.2023.2273418





2023 SANIBEL PROCEEDINGS



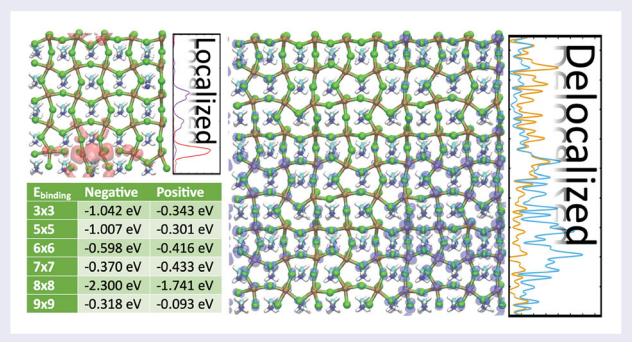
Size effects on polaron formation in lead chloride perovskite thin films

David R. Graupner David R. Graupner David R. Graupner

Department of Chemistry and Biochemistry, North Dakota State University, Fargo, ND, USA

ABSTRACT

Lead halide perovskites (LHP) are of interest for light-emitting applications due to the tunability of their bandgap across the visible and near-infrared spectrum (IR) coupled with efficient photoluminescence quantum yields (PLQY). It is widely speculated that photoexcited electrons and holes spatially separate into large negative (electron) and positive (hole) polarons. Polarons are expected to be optically active. With the observed optoelectronic signatures expecting to show potential excited states within the polaronic potential well. From the polaron excited-state we predict that large polarons should be capable of spontaneous emission, photoluminescence, in the mid-IR to far-IR regime based on the concept of inverse occupations within the polaron potential well. Here we use density functional theory (DFT), including spin-orbit coupling interactions, for calculations on a two-dimensional Dion-Jacobson (DJ) lead chloride perovskite atomistic model of various sizes as a host material for either negative or positive polarons to examine the effects of size on polaron formation. This work provides computational evidence that polaron formation through selective charge injection does not show the same level of localisation for positive and negative polarons.



ARTICLE HISTORY

Received 9 May 2023 Accepted 17 October 2023

KEYWORDS

Two-dimensional Dion-Jacobson lead halide perovskite: polaron formation; polaron localization

1. Introduction

Factors such as ground-state electronic structure, interactions between interfaces of layers, light-matter interactions, and the radiative and nonradiative dynamics of charge-carriers in the excited-state determine the performance of solid-state optoelectronic devices, such as light-emitting diodes (LEDs), lasers, and photovoltaic cells affect the performance of devices. Engineering the performance of optoelectronic devices requires knowledge on how to tune features of electronic structures, such as enhancing radiative recombination kinetics of chargecarriers using confinement for LEDs and maximising the absorbance power density in photovoltaics.

 $APbX_3$ (A = methylammonium (MA), formamidi nium (FA), Cs; X = Cl, Br, I) lead halide perovskites

(LHPs) are a type of material that have shown promise for photovoltaics [1–3] and LEDs [4–6]. The reasons LHPs show promise for next generation optoelectronic devices is due to their high quantum yields [7], high colour purity [8], tuneable emission over the visible spectrum [9], and low cost [10]. Three-dimensional (3D) LHP bulk materials show poor stability when exposed to moisture or photoirradiation [11,12]; this has led to the examination of two-dimensional (2D) inorganic-organic hybrid perovskites which offer increased stability [13]. 2D The Ruddlesden-Popper (RP) phase [14] and Dion-Jacobson (DJ) phase [15,16] being commonly studied structures of LHPs. The thickness of the perovskite layer (n perovskite octahedra) and relative stacking of the perovskite layers is used to categorise 2D LHPs with the DJ perovskites



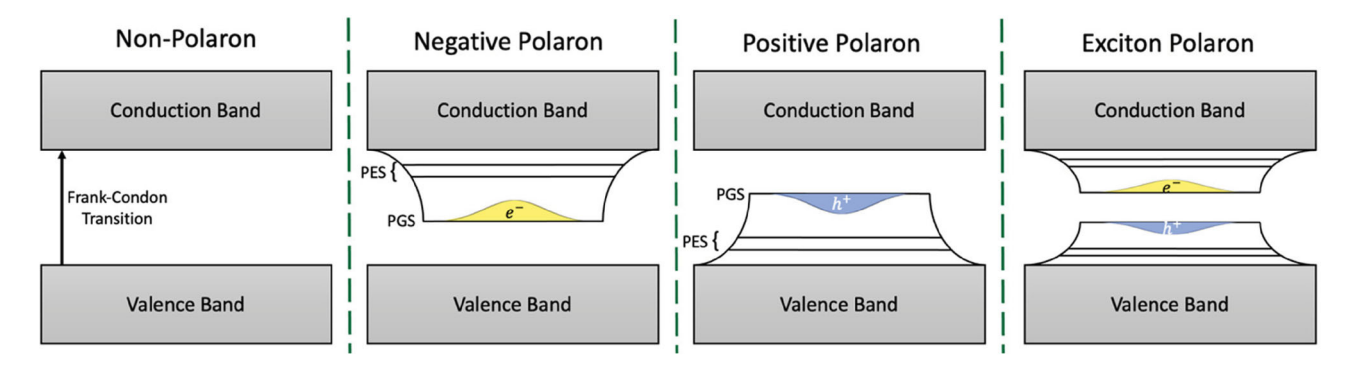


Figure 1. Schematic representation of polaron formation on band structure.

exhibiting an offset of (0,0) between perovskite layers due to the divalent organic spacers while the RP perovskites show an offset of (1/2,1/2) [17].

Polarons are quasi-particles formed due to the static coupling of nuclear and electronic degrees of freedom that are typically observed in polar crystals [18]. The Fröhlich Hamiltonian [19] is used to describe polarons. Polarons have an electronic structure with the lowest polaron energy state being the polaron groundstate (PGS) and the next highest energy state being the polaron excited- state (PES), as illustrated in the schematic in Figure 1. Polarons are also expected to be optically active [20] with transient absorption experiments observing infrared absorption characteristics [21]. There are two mechanisms for the creation of polaronic states: a selective charge injection producing single polarons, or bipolarons with the same charge, or a photoexcitation producing a simultaneous electron (negative) and hole (positive). Once the charges are introduced to the lattice, polaron formation can be described by the static coupling of electronic and nuclear degrees of freedom within the Born—Oppenheimer (BO) approximation (diagonal matrix elements of the BO Hamiltonian). Here we use density functional theory (DFT) based computational methodology [22-24] to model polaron formation on n = 1 DJ lead chloride perovskites of varying sizes to determine the model size that shows properties that could indicate that polaron may be a potential infrared photoluminescence source.

2. Methods

2.1. Ground-State electronic structure calculations

Noncollinear spin DFT [25,26] is used as the electronic basis, and we include the spin-orbit coupling (SOC) interaction due to the large angular momentum of conduction band Pb²⁺ 6p orbitals. A self-consistent noncollinear spin DFT uses four densities $\rho_{\sigma\sigma'}(\vec{r})$ and rests

on the Kohn-Sham (KS) equation.

$$\sum_{i,\sigma'=\alpha,\beta} (-\delta_{\sigma\sigma'} \nabla^2 + \nu_{\sigma\sigma'}^{eff}[\rho_{\sigma\sigma'}(\vec{r})]) \varphi_{i\sigma}(\vec{r}) = \varepsilon_i \, \varphi_{i\sigma'}(\vec{r})$$

In eq. 1, $v_{\sigma\sigma'}^{eff}[\rho_{\sigma\sigma'}(\vec{r})]$ is the 2×2 matrix operator of effective potential and α and β are orthogonal spin indices. In accordance with the self-consistent Kohn–Sham theorem, the 2×2 effective potential is a functional of the electronic density for an N electron system $v_{\sigma\sigma'}^{eff} = \frac{\delta E^{TOT}[\rho_{\sigma\sigma'}^N]}{\delta \rho_{\sigma\sigma'}^N}$. The forces acting on the nuclei changes as the total number of electrons, $N \pm \Delta N$, change due to having a new electronic density $\rho_{\sigma\sigma'}^{N\pm\Delta N}$.

Solutions of eq. 1 produce spinor Kohn–Sham orbitals (SKSOs), which are two component wavefunctions composed of a superposition of $|\alpha\rangle$ and $|\beta\rangle$ spin components.

$$\varphi_i^{SKSO}(\vec{r}) = \begin{cases} \varphi_{i\alpha}(\vec{r}) \\ \varphi_{i\beta}(\vec{r}) \end{cases} = \varphi_{i\alpha}(\vec{r})|\alpha + \varphi_{i\beta}(\vec{r})|\beta \qquad (2)$$

Within the noncollinear spin DFT framework, relativistic effects can be incorporated using second-order scalar relativistic corrections.

$$H^{relativistic} = H^{SR} + H^{SOC} \tag{3}$$

 H^{SR} is the scalar relativistic term and H^{SOC} is the SOC term. The H^{SR} term describes relativistic kinetic energy corrections and H^{SOC} describes energy shifts of spin occupations. Up to the second-order, H^{SOC} is represented as

$$H^{SOC} = \frac{\hbar}{4m^2c^2} \frac{1}{r} \frac{\partial v_{sphere}^{KS}}{\partial r} \vec{L} \cdot \vec{S}$$
 (4)

where \vec{L} is the angular momentum operator and \vec{S} is composed of Pauli spin matrices.

The optimised geometry of the charge neutral model was determined within the self-consistent DFT with N number of electrons as a starting point. This corresponds to transforming the Fröhlich Hamiltonian

[27], $H_{polaron} = H_e + H_{ph} + H_{e-ph}$, terms to a mixed quantum-classical methodology.

$$H_e^N(\vec{r}) + H_{ph}(\vec{R}) + H_{e-ph}^{static}(\vec{r}, \vec{R}) = H_{SKSO}^N(\vec{r}, \vec{R})$$
 (5)

 $H_{SKSO}^{N}(\vec{r}, \vec{R})$ describes the nuclear and electronic degrees of freedom where the total energy depends parametrically on the nuclear coordinates.

Polaronic states were described by adding or removing a charge ΔN from the N electron system to give $N \pm \Delta N$ electrons. The ions are not allowed to reorganise around the new charge density $\rho_{\sigma\sigma'}^{N\pm\Delta N}$, keeping the nuclear coordinates from the N electron system.

$$H_e^{N\pm\Delta N}(\vec{r}) + H_{ph}(\vec{R}) + H_{e-ph}^{static}(\vec{r}, \vec{R}) = H_{SKSO}^{N\pm\Delta N}(\vec{r}, \vec{R})$$
(6)

This is analogous to a Franck-Condon transition from the ground-state potential energy surface to the lowestexcited state potential energy surface. Then the nuclei are allowed to reorganise around the charge density $\rho_{\sigma\sigma'}^{N\pm\Delta N}$,

$$H_e^{N \pm \Delta N}(\vec{r}) + H_{ph}(\vec{R}) + H_{e-ph}^{static}(\vec{r}, \vec{R})$$

$$= H_{SKGO}^{N \pm \Delta N}(\vec{r}, \vec{R} + \delta \vec{R})$$
(7)

with δR being the change in nuclear coordinates. This corresponds to finding the minima of the lowest-excited state potential energy surface. The electron - phonon interaction of the Fröhlich Hamiltonian is approximated by subtracting eq 6 from eq 7.

$$H_{e-ph}^{N\pm\Delta N}(\vec{r},\vec{R}) = H_{SKSO}^{N\pm\Delta N}(\vec{r},\vec{R}+\delta\vec{R}) - H_{SKSO}^{N\pm\Delta N}(\vec{r},\vec{R})$$
(8

This describes the reorganisation energy form the Franck-Condon states to the minima on the excited-state potential energy surface.

2.2. Ground-State observables

The binding energy was calculated for each model using eq. 9,

$$E_{binding} = E_{polaron}^{N \pm \Delta N} - E_{FC}^{N \pm \Delta N} \tag{9}$$

where $E_{FC}^{N\pm\Delta N}$ is the total energy of the charged system where the nuclei were not allowed to reorganise and $E_{polaron}^{N\pm\Delta N}$ is the total energy of the charged system where the nuclei were allowed to reorganise.

For each model, we computed the electronic density of states DOS as.

$$DOS_{SKSO} = \sum_{i} \delta(\varepsilon - \varepsilon_{i}^{SKSO} - \varepsilon_{Fermi})$$
 (10)

where ε_i^{SKSO} is the band eigenenergy and $\epsilon_{fermi} = \frac{\varepsilon_i^{SKSO,HOMO} + \varepsilon_i^{SKSO,LUMO}}{2}$ is the Fermi level.

We use the independent orbital approximation (IOA) [28,29] in which excited states are described as a pair of orbitals, as opposed to a superposition of orbitals commonly used in Bethe-Saltpeter or time dependent DFT (TDDFT) approaches. Optical transitions between SKSO i and i can be found through transition dipole matrix elements, eq. 11,

$$\vec{D}_{ij} = e \int d\vec{r} \left\{ \varphi_{i\alpha}^* \quad \varphi_{i\beta}^* \right\} \vec{r} \left\{ \begin{matrix} \varphi_{j\alpha} \\ \varphi_{j\beta} \end{matrix} \right\}$$
(11)

which can be used to compute oscillator strengths, eq. 12.

$$f_{ij} = |\vec{D}_{ij}|^2 \frac{4\pi \, m_e \nu_{ij}}{3\hbar e^2} \tag{12}$$

where v_{ii} represents the transition frequency between SKSO i and j. The transition frequency v_{ii} is related to the transition energy ΔE_{ij} by $h\nu_{ij} = \Delta E_{ij}$. With known oscillator strengths, an absorption spectrum can be computed through eq. 13.

$$\alpha^{SKSO}(\varepsilon) = \sum_{i < j} f_{ij} \delta(\hbar \omega - \hbar \omega_{ij}) \{ \rho_{ii}^{eq} - \rho_{jj}^{eq} \}$$
 (13)

The orbitals calculated by eq. 1 are visualised in the form of 3D iso-surfaces of partial charge density or as one-dimensional distributions by eq. 14.

$$\rho_i(z) = \iint dx dy |\varphi_i^{\text{SKSO}}(x, y, z)|^2$$
 (14)

2.3. Computational and atomistic details

DFT in a plane-wave basis set along with projector augmented-wave (PAW) pseudopotentials [30,31] with the generalised gradient approximation (GGA) Perdew-Burke-Ernzerhof (PBE) functional [32] in Vienna Ab initio Simulation Package (VASP) [33] software was used to calculate the ground-state electronic structure of our atomistic model. Observables were computed using subsequent single point calculations performed using noncollinear spin DFT including the SOC interaction for all systems. While it is known that PBE-SOC calculations can underestimate the bandgap in LHPs, it is important to consider due to the large angular momentum of the Pb 6p orbitals [34,35]. All calculations were performed at the Γ point.

The periodic model is created from the bulk CsPbCl₃ crystal structure, n'xn'x1 unit cells was carved out, n' = 3,5,6,7,8,9, giving three Cl/Cs terminated surfaces and three Pb/Cl terminated surfaces providing a composition of $Cs_{n'^2}Pb_{n'^2}Cl_{3n'^2}$. The Cs atoms are removed from the perovskite structure and replaced with 1,4butanediammonium (BdA) molecules. Cl atoms are then

added on the opposite end of the BdA molecules in line with the octahedral Pb/Cl structures from the initial crystal structure [36]. Overall, this gives a structure of BdA_{n'2}Pb_{n'2}Cl_{4n'2}. Atomistic models for the pristine models can be observed in Figure 2 and Figure S1 and for the polaronic models in Figures S4-S9, all atomistic models shown here are viewed along the y-axis as indicated in Figure 2. A view of how the BdA molecules are attached to the LHP is shown Figure S2 for the pristine models. An odd n' will lead to a defected state due to the mismatch of the octahedral splitting [37], but we are including these values in a systemic search of target models.

The charge neutral ground-state structure is optimised using a N electron system. To model polaron formation, we replace a Pb ion with either a Tl or Bi ion and reoptimize the structure. The Tl/Bi ion is replaced with a Pb ion and ΔN electrons are added/removed from the system and reoptimize the structure using the charge density from the doped model. The spurious electrostatic interactions between replicas of charged species [38] are avoided with the use of a background charge concept

Constrained DFT was implemented to explore the electronic and optical properties of various spin multiplicity polaronic states. Within spin-polarised DFT, we specify the number of α and β electrons from the spindependent electronic density ρ_{σ} to have $N_{\alpha} = \int \rho_{\alpha} dr^3$ and $N_{\beta} = \int \rho_{\beta} dr^3$. The spin state $s = \frac{\delta N}{2}$ and multiplicity m = 2s + 1 is defined by their difference $\delta N = N_{\alpha}$ – N_{β} . We explored singlet (m = 1), doublet (m = 2), and triplet (m = 3) spin multiplicities. Note that $N_{\alpha} + N_{\beta}$ defines the total number of electrons and is different for positive and negative polarons. The noncollinear spin DFT charge density was constrained to have a specified multiplicity from the spin-polarised charge density.

3. Results

Figure 3 shows the ground-state density of states (DOS) for the valence band of the pristine and positive polaron models. The energy axis has been normalised to the Fermi energy of the pristine model. The DOS for the pristine models valence band shows a similar peak pattern for the 7×7 and 8×8 model while the smaller models show an additional peak and the 9×9 model shows one less peak. The loss of the shoulder near $-1.5 \,\text{eV}$ in the DOS for the 9×9 model is attributed to mismatch of the octahedral tilting due to odd n' [37]. This mismatch leads to an artificial breaking of the octahedral tilting across the periodic boundary which alters the electronic properties of the LHP. The polaronic models, as a result of hole injection, exhibit the valence band maximum having a higher energy than in the models without hole injection. This

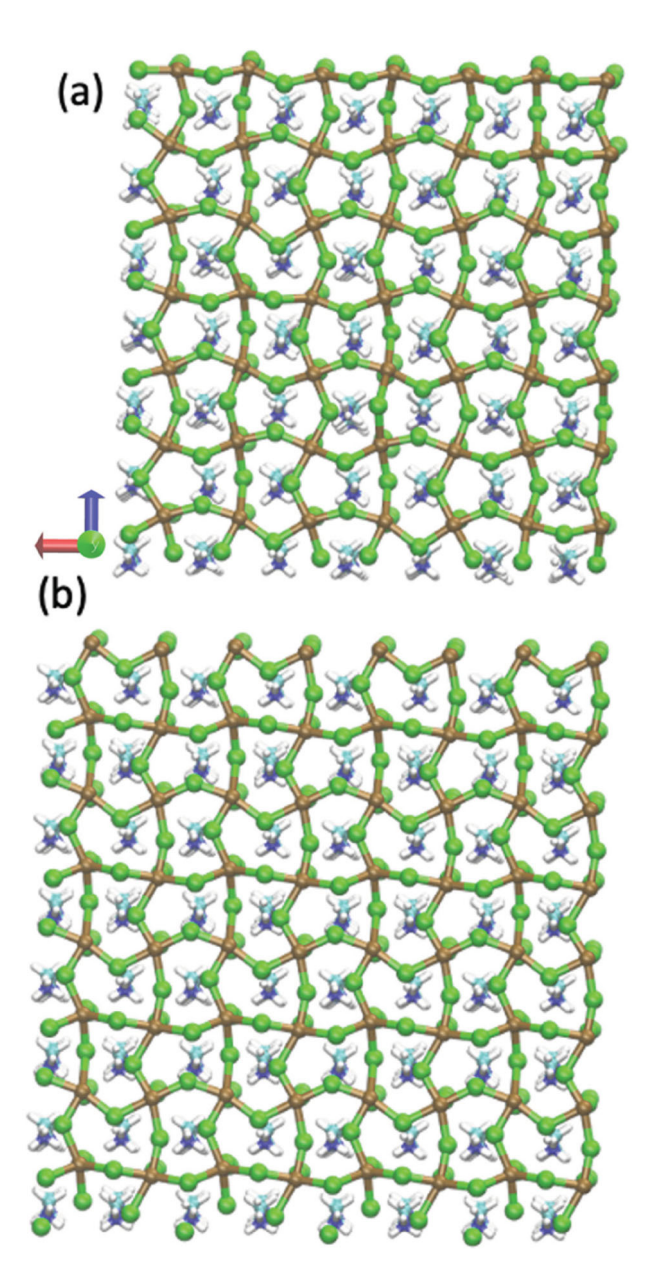


Figure 2. Atomistic models for the pristine (a) 7×7 and (b) 8 × 8 lead chloride perovskites viewed along the y-axis. White, cyan, blue, brown, and green spheres represent hydrogen, carbon, nitrogen, lead, and chlorine atoms respectively. Note that the octahedral tilting in the 7×7 model is disrupted by the periodic boundary, with the tilting in the octahedra along the upper and right periodic boundaries being flatter than in the 8×8 model. Atomistic models for other examined pristine unit cell sizes can be seen in Figure S1.

is most noticeable in the 3×3 and the 8×8 models as there is little change in the shape of the DOS for all models except the 3×3 ; we attribute this to the lack coverage of the Brillouin zone in the Γ point calculation.

The conduction band DOS for the pristine and negative polarons, shown in Figure 4, exhibit similar results to the valence band DOS. The pristine model DOS exhibits a similar peak pattern for all models except the 3×3 size.

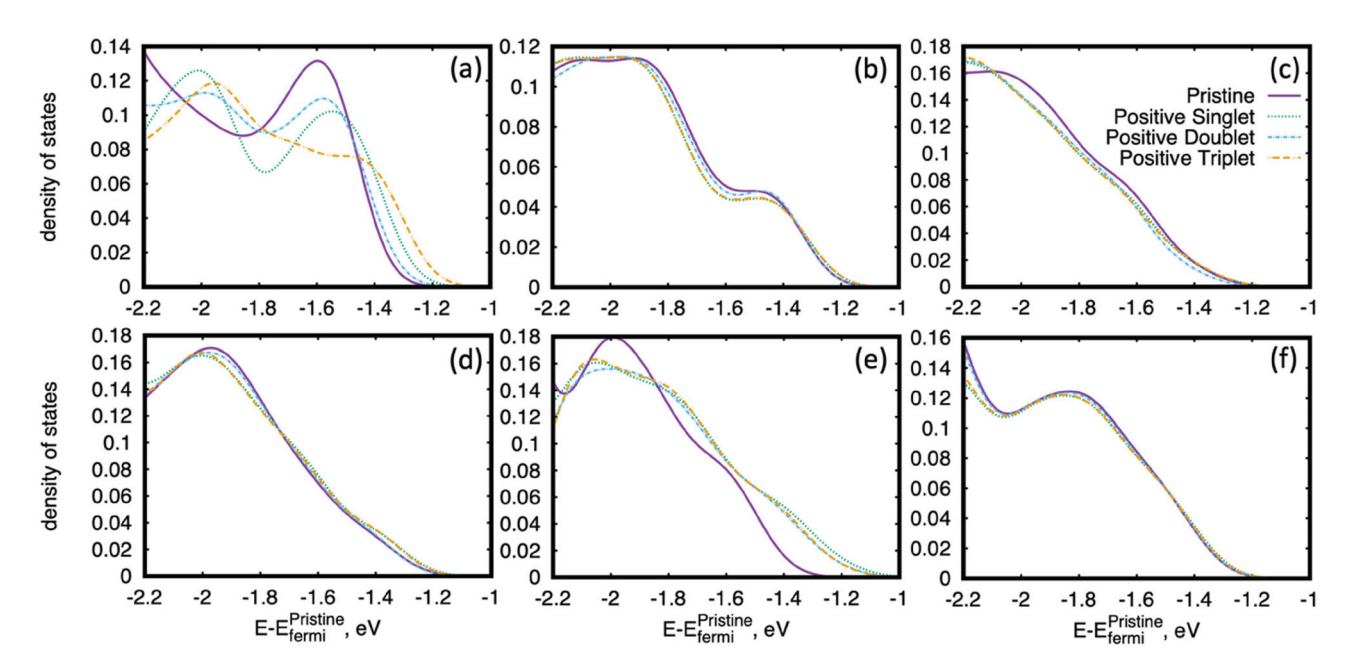


Figure 3. Valence band density of states for pristine perovskite (purple, solid), singlet positive polaron (green, dot), doublet positive polaron (blue, dash-dot), and triplet positive polaron (yellow, dot-dash-dot) with model sizes of (a) 3×3 , (b) 5×5 , (c) 6×6 , (d) 7×7 , (e) 8×8 , and (f) 9×9 . The energy has been normalised to the Fermi energy of the pristine model. It is observed that for all sizes, the polaronic models exhibit bands that are within the pristine bandgap. Qualitatively, the shape of the density of state is consistent for all models larger than 3×3 .

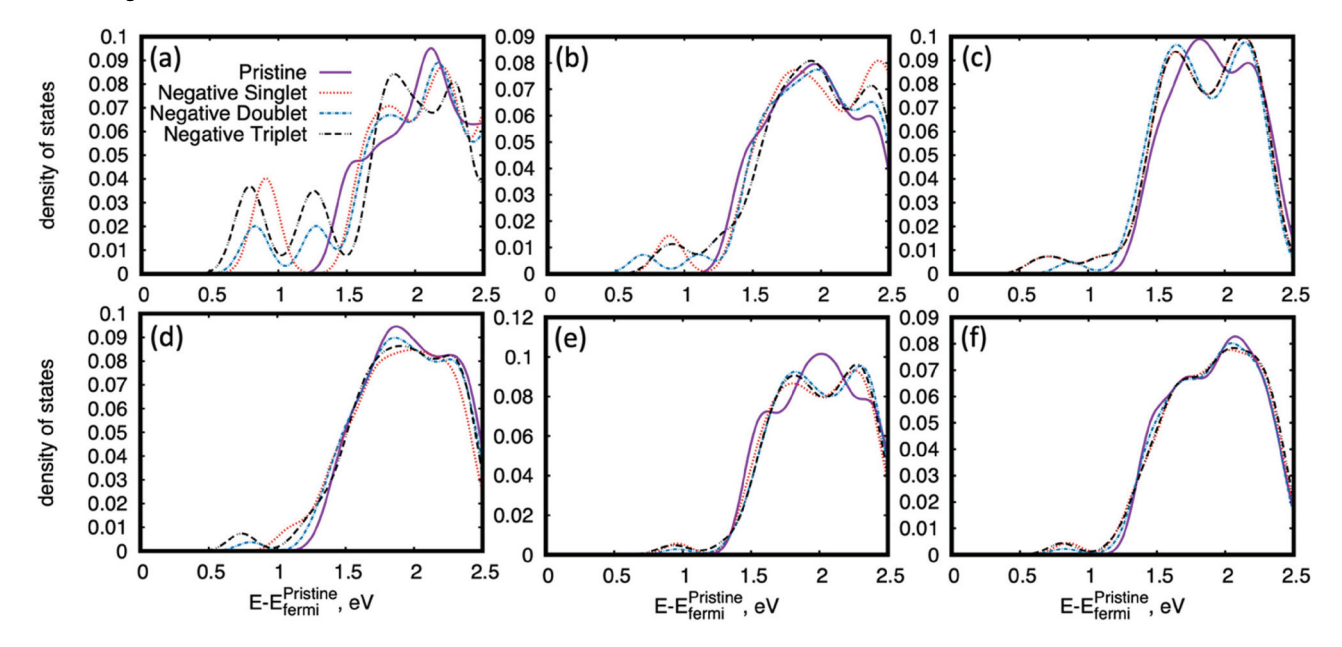


Figure 4. Conduction band density of states for pristine (purple, solid), singlet negative polaron (red, dot), doublet negative polaron (blue, dash-dot), and triplet negative polaron (black, dot-dash-dot) with model sizes of (a) 3×3 , (b) 5×5 , (c) 6×6 , (d) 7×7 , (e) 8×8 , and (f) 9×9 . The energy has been normalised to the Fermi energy of the pristine model. It is observed that for all sizes, the polaronic models exhibit bands that are within the pristine bandgap.

The difference between the DOS for the 3×3 model and the other models is attributed to the lack coverage of the Brillouin zone in the Γ point calculation. The conduction band minimum for the polaronic models, due to electron injection, is lower in energy than for the pristine model. Additionally, the polaronic states show a distinct peak in

the conduction band DOS, unlike the valence band DOS for the positive polarons.

Figure 5 shows the computed absorption spectra for the models studied. The polaronic models show good agreement for absorption arising from transitions that do not involve polaronic states to the pristine absorption.

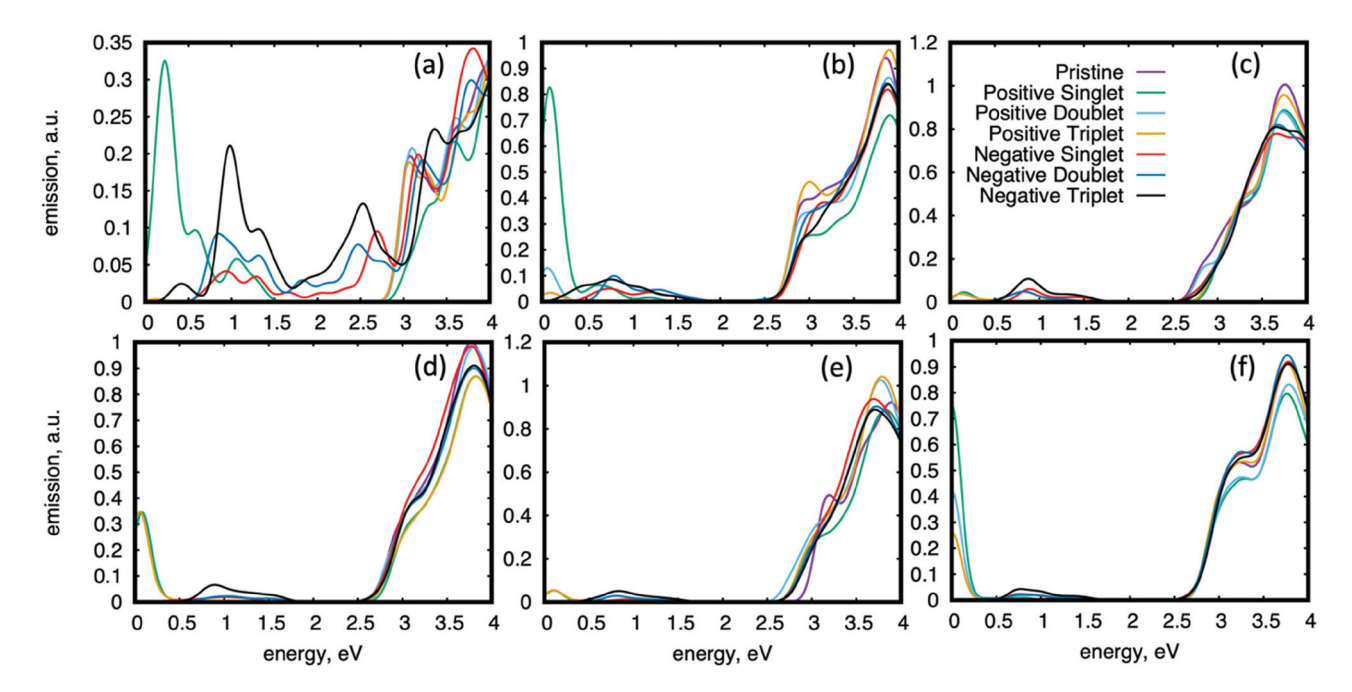


Figure 5. Computed absorption spectra for pristine perovskite (purple), singlet positive polaron (green), doublet positive polaron (light blue), triplet positive polaron (yellow), singlet negative polaron (red), doublet negative polaron (dark blue), and triplet negative polaron (black) with model sizes of (a) 3×3 , (b) 5×5 , (c) 6×6 , (d) 7×7 , (e) 8×8 , and (f) 9×9 .

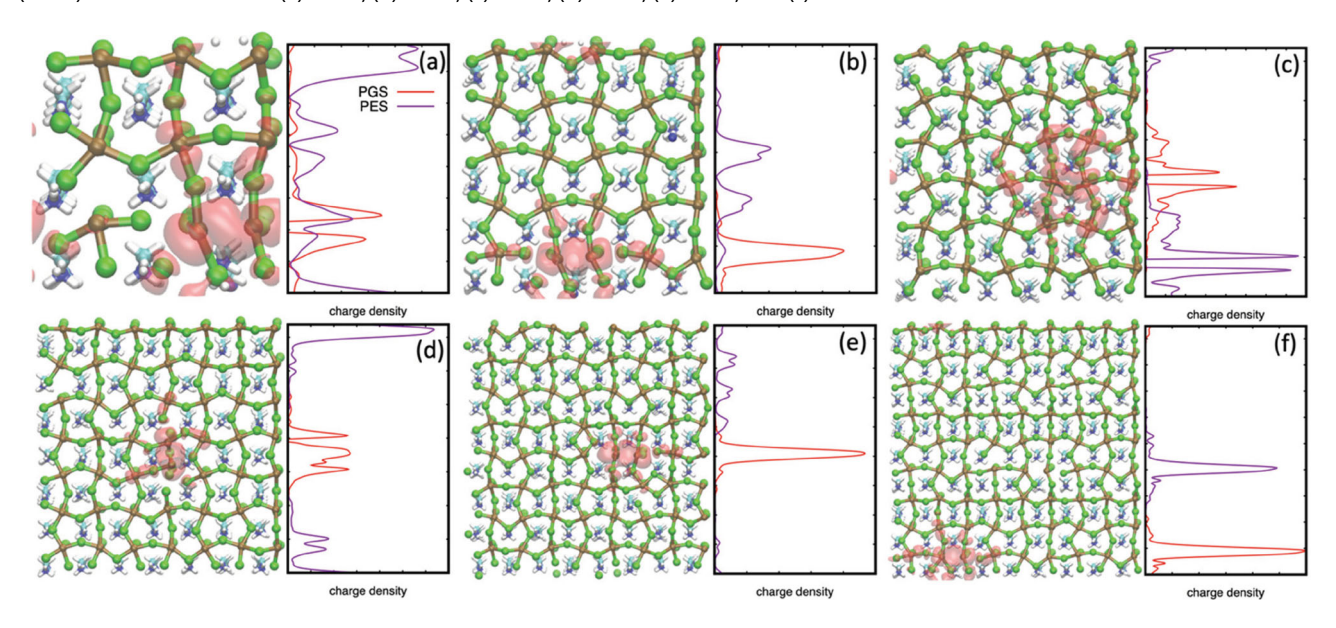


Figure 6. SKSOs for the singlet negative polaron (a) 3×3 , (b) 5×5 , (c) 6×6 , (d) 7×7 , (e) 8×8 , and (f) 9×9 lead chloride perovskites. The PGS is represented in red and PES in purple. The left figure in each panel shows the 3D iso-surfaces of partial charge density for the PGS while the right figure in each panel shows the one-dimensional distributions for the PGS and PES. The PGS is seen to be localised to an area of two octahedra in radius for the negative polaron models.

Absorption lower in energy than the pristine results from the charge injection forming polaronic states. Absorption involving positive polaronic states occurs at less than $0.5\,\text{eV}$ for models larger than 5×5 . While absorption involving negative polaronic states occurs between 0.5 and 1.5 eV for models larger than 5×5 . For smaller models the absorption due to polaronic states occurs across a wider energy range.

Another factor to consider for the formation of polarons is the localisation of the SKSO within the model. SKSOs for the singlet negative polaron models are shown in Figure 6. The left figure in each panel shows the threedimensional (3D) iso-surfaces of partial charge density for the PGS while the right figure in each panel shows the one-dimensional (1D) distributions for the PGS and PES. The PGS is represented in red and PES in purple.

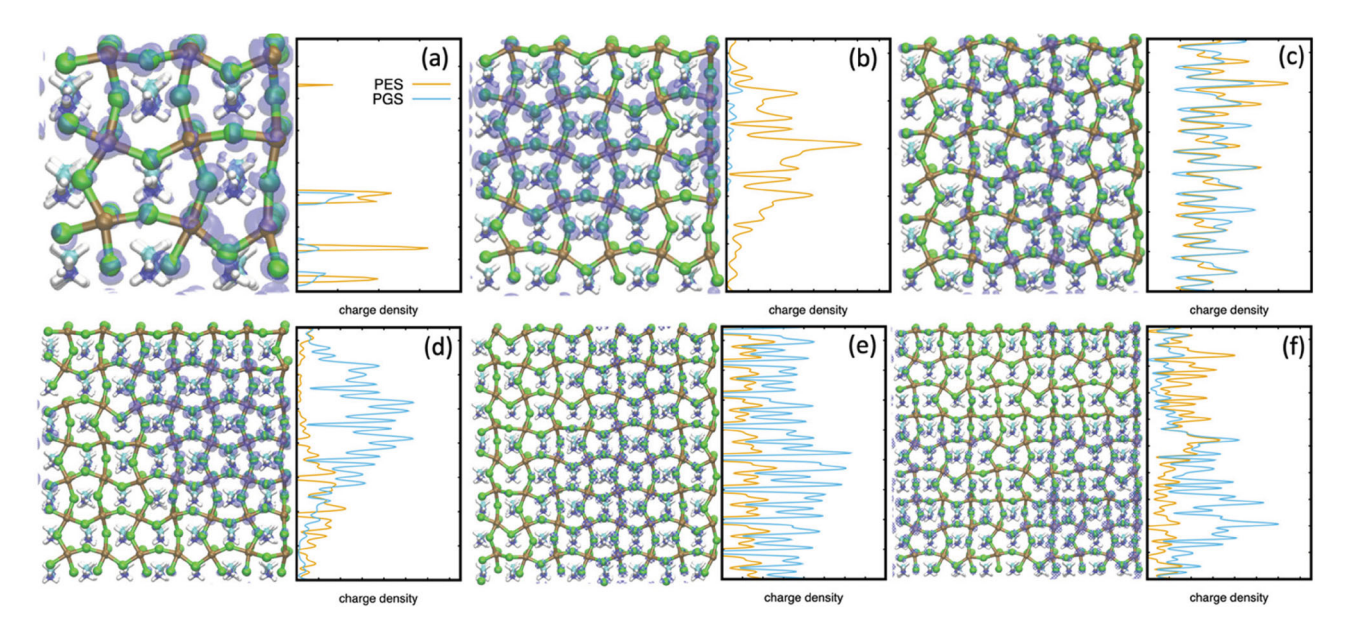


Figure 7. SKSOs for the singlet positive polaron (a) 3×3 , (b) 5×5 , (c) 6×6 , (d) 7×7 , (e) 8×8 , and (f) 9×9 lead chloride perovskites. The PGS is represented in blue and PES in orange. The left figure in each panel shows the 3D iso-surfaces of partial charge density for the PGS while the right figure in each panel shows the one-dimensional distributions for the PGS and PES. The PGS does not localise in a specific region of the perovskite layer for the positive polaron models.

Table 1. Polaronic binding energy calculated using eq. 9.

	Negative singlet	Negative doublet	Negative triplet	Positive singlet	Positive doublet	Positive triplet
3 × 3	−1.042 eV	−0.304 eV	−0.625 eV	−0.343 eV	−0.100 eV	−0.387 eV
5×5	−1.007 eV	−0.388 eV	−0.457 eV	−0.301 eV	$-0.090\mathrm{eV}$	$-0.299\mathrm{eV}$
6×6	$-0.598\mathrm{eV}$	−0.333 eV	$-0.598\mathrm{eV}$	$-0.416\mathrm{eV}$	$-0.336\mathrm{eV}$	$-0.398\mathrm{eV}$
7×7	$-0.370\mathrm{eV}$	0.007 eV	−0.465 eV	$-0.433\mathrm{eV}$	−0.241 eV	$-0.490\mathrm{eV}$
8×8	−2.300 eV	−1.842 eV	−1.919 eV	−1.741 eV	−1.578 eV	−1.514 eV
9×9	−0.318 eV	−0.263 eV	$-0.404\mathrm{eV}$	$-0.093\mathrm{eV}$	$-0.024\mathrm{eV}$	−0.083 eV

For all negative polaron models, the PGS is seen to be localised to an area two perovskite octahedra in radius for the negative polaron models. The 1D distributions of the SKSO exhibit a similar trend for the PGS, with the charge density being localised to a small region of the model. The SKSOs for the singlet positive polaron models are shown in Figure 7. The PGS is represented in blue and PES in orange while the rest of the format is the same as for Figure 6. Unlike for the negative polaron models, in the positive polaron models the PGS does not localise in a specific region of the perovskite layer. the SKSOs and 1D distributions for the doublet and triplet multiplicity models exhibit the same trends as for the singlet multiplicities as seen in Figures S9-S12.

Table 1 shows the polaron binding energy calculated by eq. 9. The 8×8 unit cell size shows the most favourable binding energy for all multiplicities and charge injections studied. The doublet multiplicity tends to be the least stable multiplicity for each size and charge. For the negative polaron models the singlet multiplicity tends to be more stable than the triplet multiplicity, while for the positive polarons the singlet and triplet multiplicities tend to have similar values for binding energy. The

negative polaron doublet 7×7 model is the only model to show an unfavourable binding energy.

4. Discussion

While it known the PBE-SOC can underestimate band gap which can be improved by using a hybrid functional, such as HSE06. This is however expected to provide a similar electronic structure and band alignment while greatly increasing the computational cost of the calculations [40]. Due to the large size of the models that are being used here we use PBE to reduce computational cost, further Forde *et al.* showed that PBE-SOC can have favourable cancellation of errors for bandgap in LHP models [28].

Examining the SKSOs, we can see that for the negative polaron models there is charge density localisation. This is indicating the successful formation of polarons in the electron injected models. However, for the positive polaron models the SKSOs show that the charge density is delocalised over the perovskite structure in a manner that is reminiscent of 2D particle in a box state. This may indicate that polarons are not forming when using the

hole injected models. The formation of polarons requires the static coupling of vibrational modes to free charges. The main contribution to polaron formation in APbX₃ perovskites will come from the reorientation of the A⁺ cations and the reorganisation of the PbX₆²⁻ octahedra, with one experiment indicating that the polaron reorganisation energy are more dependent on the A⁺ cation composition than halide composition [37]. The use of the DJ linker molecule as the A⁺ cation may inhibit the lattice reorganisation due to the charge injection.

The 8 \times 8 unit cells shows the most favourable binding energies for all system sizes due to the even values of primitive unit cells allowing for the model to exhibit the octahedral tilting that is expected for an orthorhombic perovskite thin film [37,41]. The greater favorability of the 8 \times 8 model over the 6 \times 6 model is attributed to the increased coverage of the Brillouin zone in the Γ point calculation. While the unfavourability of the negative polaron with doublet multiplicity for the 7 \times 7 model is attributed to the less favourable formation of the doublet multiplicity [22] and the poor overlap of the octahedral tilting across the periodic boundary. In general, the positive polaron models exhibit binding energies that are favourable to recent results for lead bromide perovskites which occur on the order of 100 meV [37].

5. Conclusion

Examining the formation of polarons in 2D lead chloride perovskites is one of the major goals in this work. To this end, we use density functional theory to explore the effects of the size of perovskite layer on the localisation and binding energy of positive and negative polarons and show that electrons tend to bind more strongly than holes in the LHP lattice. The charge density localisation and radial distribution function indicate that polarons are forming when elections are injected into the n = 1Dion-Jacobson lead chloride perovskite. This indicates that the negative polaron models are good choices to use for continued work with excited-state dynamics to determine nonradiative and radiative rates of recombination. These additional calculations will indicate whether polarons in two-dimensional lead chloride perovskites may have potential as infrared emission sources. However, it is seen that polaron formation due to hole injection into n = 1 Dion-Jacobson lead chloride perovskite does not lead to the expected charge localisation for a polaronic state. Additional studies must be performed to determine the reason that the positive polaron is not forming in these models.

The binding energies calculated for polaron formation indicate that the models with an n'xn' unit cell where n is even show a decreased energy when compared to

the unit cells where n' is odd. The difference in binding energy due to the even or oddness of the sides of the unit cell is attributed to a mismatch of the atomic positions across the periodic boundary of the model due to the octahedral tilting in orthorhombic perovskites. This is indicating that for future studies of this material, computations should be performed on a model with a unit cell that is n'xn' where n' is even with n' = 8 showing the greatest potential for further study.

Acknowledgements

DRG thanks NSF CHE- 2004197. DSK thanks NSF CHE-1944921. This research used resources of the National Energy Research Scientific Computing Center (NERSC), a U.S. Department of Energy Office of Science User Facility located at Lawrence Berkeley National Laboratory, operated under Contract No. DE-AC02-05CH11231 using allocation award m1251 for 2023, "Computational Modeling of Photo-catalysis and Photo-induced Charge Transfer Dynamics on Surfaces". We also thank Aaron Forde, Yulun Han, Dinesh Thapa, Landon Johnson, Adam Flesche, Steven Westra, Kamrun Keya, Sarah Ghazanfari, Meade Ericson, Hadassah Griffin, Amara Arshad, Joseph Granlie, William Tupa, and Patricia Adeoye for collective discussion and editing.

Disclosure statement

No potential conflict of interest was reported by the author(s). This work was supported by Basic Energy Sciences: [Grant Number DE-AC02-05CH11231]; National Science Foundation: [Grant Number 1944921].

ORCID

David R. Graupner http://orcid.org/0000-0003-3879-8559 Dmitri S. Kilin http://orcid.org/0000-0001-7847-5549

References

- [1] W. Nie, H. Tsai, R. Asadpour, J.-C. Blancon, A.J. Neukirch, G. Gupta, J.J. Crochet, M. Chhowalla, S. Tretiak, M.A. Alam, H.-L. Wang and A.D. Mohite, Science. **347** (6221), 522 (2015). doi:10.1126/science.aaa0472.
- [2] L. Yang, X. Wang, X. Mai, T. Wang, C. Wang, X. Li, V. Murugadoss, Q. Shao, S. Angaiah, and Z. Guo, J. Colloid Interface Sci. 534, 459 (2019). doi:10.1016/j.jcis.2018.09.045
- [3] Y. Huang, Z. Yuan, J. Yang, S. Yin, A. Liang, G. Xie, C. Feng, Z. Zhou, Q. Xue, Y. Pan, F. Huang and Y. Chen, Sci. China Chem. 66 (2), 449–458 (2023). doi:10.1007/s11426-022-1436-7.
- [4] J. Song, J. Li, X. Li, L. Xu, Y. Dong and H. Zeng, Adv. Mater. **27** (44), 7162 (2015). doi:10.1002/adma.201502567.
- [5] K. Lin, J. Xing, L.N. Quan, F.P.G. de Arquer, X. Gong, J. Lu, L. Xie, W. Zhao, D. Zhang, C. Yan, W. Li, X. Liu, Y. Lu, J. Kirman, E.H. Sargent, Q. Xiong and Z. Wei, Nature. 562 (7726), 245 (2018). doi:10.1038/s41586-018-0575-3.
- [6] M.H. Park, Materials. 15 (13), 4571 (2022). doi:10.3390/ ma15134571.



- [7] Y. Miao, L. Cheng, W. Zou, L. Gu, J. Zhang, Q. Guo, Q. Peng, M. Xu, Y. He, S. Zhang, Y. Cao, R. Li, N. Wang, W. Huang and J. Wang, Light Sci. Appl. 9 (1), 89 (2020). doi:10.1038/s41377-020-0328-6.
- [8] M. Alahbakhshi, A. Mishra, G. Verkhogliadov, E.E. Turner, R. Haroldson, A.C. Adams, Q. Gu, J.J. Rack, J.D. Slinker and A.A. Zakhidov, Adv. Funct. Mater. 2214315 (2023). doi:10.1002/adfm.202214315.
- [9] L. Protesescu, S. Yakunin, M.I. Bodnarchuk, F. Krieg, R. Caputo, C.H. Hendon, R.X. Yang, A. Walsh and M.V. Kovalenko, Nano Lett. 15 (6), 3692 (2015). doi:10.1021/ nl5048779.
- [10] J.J. Wang, D.Y. Li, L. Mu, M.Z. Li, Y. Luo, B.B. Zhang, C.H. Mai, B.A. Guo, L.F. Lan, J. Wang, H.L. Yip and J.B. Peng, ACS Appl. Mater. Interfaces. 13 (35), 41773-41781 (2021). doi:10.1021/acsami.1c07526.
- [11] E.-B. Kim, M.S. Akhtar, H.-S. Shin, S. Ameen and M.K. Nazeeruddin, J. Photochem. Photobiol. C. 48, 100405 (2021). doi:10.1016/j.jphotochemrev.2021.100405.
- [12] C. Ma, C. Leng, Y. Ji, X. Wei, K. Sun, L. Tang, J. Yang, W. Luo, C. Li, Y. Deng, S. Feng, J. Shen, S. Lu, C. Du and H. Shi, Nanoscale. 8 (43), 18309 (2016). doi:10.1039/C6NR04741F.
- [13] F. Arabpour Roghabadi, M. Alidaei, S.M. Mousavi, T. Ashjari, A.S. Tehrani, V. Ahmadi and S.M. Sadrameli, J. Mater. Chem. A. 7 (11), 5898 (2019). doi:10.1039/C8TA10444A.
- [14] C.C. Stoumpos, D.H. Cao, D.J. Clark, J. Young, J.M. Rondinelli, J.I. Jang, J.T. Hupp and M.G. Kanatzidis, Chem. Mater. 28 (8), 2852 (2016). doi:10.1021/acs.chem mater.6b00847.
- [15] M. Dion, M. Ganne and M. Tournoux, Mater. Res. Bull. **16** (11), 1429 (1981). doi:10.1016/0025-5408(81)90063-5.
- [16] A.J. Jacobson, J.W. Johnson and J.T. Lewandowski, Inorg. Chem. 24 (23), 3727 (1985). doi:10.1021/ic00217a006.
- [17] L. Mao, W. Ke, L. Pedesseau, Y. Wu, C. Katan, J. Even, M.R. Wasielewski, C.C. Stoumpos and M.G. Kanatzidis, J. Am. Chem. Soc. 140 (10), 3775-3783 (2018). doi:10.1021/jacs.8b00542.
- [18] C. Franchini, M. Reticcioli, M. Setvin and U. Diebold, Nat. Rev. Mater. 6 (7), 560-586 (2021). doi:10.1038/s41578-021-00289-w.
- [19] H. Fröhlich, Proc. R. Soc. London, Ser. A. 160 (901), 230-241 (1937). doi:10.1098rspa.1937.0106.
- [20] D. Emin, Phys. Rev. B. 48 (18), 13691-13702 (1993). doi:10.1103/PhysRevB.48.13691.
- [21] K.T. Munson, G.S. Doucette, E.R. Kennehan, J.R. Swartz fager and J.B. Asbury, J. Phys. Chem. C. 123 (12), 7061-7073 (2019). doi:10.1021/acs.jpcc.9b00555.

- [22] A. Forde, T. Inerbaev and D. Kilin, J. Phys. Chem. C. 124 (1), 1027-1041 (2020). doi:10.1021/acs.jpcc.9b08044.
- [23] D.R. Graupner and D.S. Kilin, MRS Adv. 7 (30), 772-777 (2022). doi:10.1557/s43580-022-00358-4.
- [24] D.R. Graupner and D. Kilin, MRS Adv. (2023). doi:10. 1557/s43580-023-00641-y.
- [25] J. Kubler, K.H. Hock, J. Sticht and A.R. Williams, J. Phys. F: Met. Phys. 18 (3), 469-483 (1988). doi:10.1088/0305-4608/18/3/018.
- [26] U.v. Barth and L. Hedin, J. Phys. C: Solid State Phys. 5 (13), 1629-1642 (1972). doi:10.1088/0022-3719/5/13/012.
- [27] J.T. Devreese and A.S. Alexandrov, Rep. Prog. Phys. 72 (6), 0066501 (2009). doi:10.1088/0034-4885/72/6/066501.
- [28] A. Forde, T. Inerbaev and D. Kilin, J. Phys. Chem. C. 122 (45), 26196 (2018). doi:10.1021/acs.jpcc.8b05392.
- [29] D.J. Vogel, A. Kryjevski, T. Inerbaev and D.S. Kilin, J. Phys. Chem. Lett. 8 (13), 3032–3039 (2017). doi:10.1021/acs. jpclett.6b03048.
- [30] G. Kresse and D. Joubert, Phys. Rev. B. **59** (3), 1758 (1999). doi:10.1103/PhysRevB.59.1758.
- [31] P.E. Blöchl, Phys. Rev. B. 50 (24), 17953-17979 (1994). doi:10.1103/PhysRevB.50.17953.
- [32] J.P. Perdew, K. Burke and M. Ernzerhof, Phys. Rev. Lett. 78 (7), 1396 (1997). doi:10.1103/PhysRevLett.78.1396.
- [33] G. Kresse and J. Furthmüller, Comput. Mater. Sci. 6 (1), 15-50 (1996). doi:10.1016/0927-0256(96)00008-0.
- [34] J. Even, L. Pedesseau, J.-M. Jancu and C. Katan, J. Phys. Chem. Lett. 4 (17), 2999–3005 (2013). doi:10.1021/ jz401532q.
- [35] T. Das, G. Di Liberto and G. Pacchioni, J. Phys. Chem. C. **126** (4), 2184–2198 (2022). doi:10.1021/acs.jpcc.1c09594.
- [36] D. R. Graupner and D. S. Kilin, J. Appl. Spectrosc. 90 (2), 436-447 (2023). doi:10.1007/s10812-023-01551-5.
- [37] A.J. Neukirch, I.I. Abate, L. Zhou, W. Nie, H. Tsai, L. Pedesseau, J. Even, J.J. Crochet, A.D. Mohite, C. Katan and S. Tretiak, J. Phys. Chem. Lett. 9 (24), 7130 (2018). doi:10.1021/acs.jpclett.8b03343.
- [38] J. Neugebauer and M. Scheffler, Phys. Rev. B. 46 (24), 16067-16080 (1992). doi:10.1103/PhysRevB.46.16067.
- [39] G. Makov and M.C. Payne, Phys. Rev. B. 51 (7), 4014-4022 (1995). doi:10.1103/PhysRevB.51.4014.
- [40] A. Forde and D. Kilin, J. Phys. Chem. C 121 (37), 20113-20125 (2017). doi:10.1021/acs.jpcc.7b04961
- [41] D. Ghosh, P. Walsh Atkins, M.S. Islam, A.B. Walker and C. Eames, ACS Energy Lett. 2 (10), 2424-2429 (2017). doi:10.1021/acsenergylett.7b00729.